

The role of tip size and orientation, tip–surface relaxations and surface impurities in simultaneous AFM and STM studies on the TiO₂(110) surface

Henry P Pinto¹, Georg H Enevoldsen², Flemming Besenbacher²,
Jeppe V Lauritsen² and Adam S Foster^{1,3}

¹ Laboratory of Physics, Helsinki University of Technology, PO Box 1100, FIN-02015, Finland

² Interdisciplinary Nanoscience Center (iNANO) and Department of Physics and Astronomy, University of Aarhus, Denmark

³ Department of Physics, Tampere University of Technology, PO Box 692, FIN-33101, Finland

E-mail: adam.foster@tut.fi and jvang@phys.au.dk

Received 29 January 2009, in final form 20 April 2009

Published 10 June 2009

Online at stacks.iop.org/Nano/20/264020

Abstract

In this work we investigate some of the key factors in simultaneously recorded scanning tunneling microscopy (STM) and non-contact atomic force microscopy (nc-AFM) images of the TiO₂(110) surface, particularly the role of tip size and orientation in the obtained contrast pattern, and the importance of tip–surface relaxations and surface impurities in measured currents. We show that, while using multi-channel scanning modes provides an increase in physical data from a given measurement and greatly aids in interpretation, it also demands much greater rigor in simulations to provide a complete comparison.

(Some figures in this article are in colour only in the electronic version)

1. Introduction

The use of simultaneously recorded multi-channel scanning probe microscopy (SPM) offers a powerful technique for characterization of surfaces and adsorbed species. Combining techniques removes many of the interpretation difficulties present when a single channel is used and provides access to a much wider selection of physical information [1, 2]. A common approach is to use feedback on force via nc-AFM, while simultaneously measuring a different signal in another channel. For example: simultaneous measurement of energy dissipation provides details of atomic jumps, force hysteresis and highlights low coordinated sites [3]; measuring the work function in Kelvin probe mode offers details of charge transfer and the local electrostatic potential [4–7]; while measuring the tunneling current probes the electronic structure of the surface and provides finer control on distance [8–10]. Multi-channel experiments provide a significant challenge for theoretical models, both in general understanding of the new

signal itself, e.g. dissipation [11] and Kelvin probe [12], and in the additional complexities introduced by combining two or more channels in a simultaneous measurement [13, 14].

The TiO₂(110) surface has always represented a benchmark metal oxide surface, and has also served as a substrate for some of the initial dual-channel studies, particularly combined STM and AFM [15]. However, both STM and AFM signals are extremely sensitive to single adsorption or desorption events on the tip or slight few-atom configuration changes in the tip structure, and the literature contains numerous examples of how the details of the contrast of even very simple surfaces may change simply as a consequence thereof. The tip structure is indeed very susceptible to changes during the experiment, and in a typical experiment the SPM operator has to modify the tip by field-induced desorption or simply by contacting the tip with the surface before stable atomic resolution is obtained, emphasizing that the tip structure and atomic composition, except in a very few cases, is unknown. In the application of

atom-resolved SPM for the analysis of the surface structure of compounds such as TiO_2 , it is a significant challenge to properly deconvolute tip effects from the real geometry of the surface [16]. However, as recently demonstrated in [14], the presence of several types of contrast in simultaneously recorded STM and nc-AFM images may be used constructively to establish an atomistic tip model by a direct comparison of the contrast details in both channels. By an analysis of the distinct signatures in the simultaneous nc-AFM and STM images, it was possible in these studies to screen a large library of Ti, Si, Si-H, Si-OH or O-terminated tips and reliably select the tip configuration which reproduced the experimental contrast on the stoichiometric parts of the surface. Going one step further, it was possible in an interplay between experiment and simulation to analyze the signatures of certain defects in simultaneous STM and AFM measurements and thereby identify them as surface OH and subsurface OH groups, both present on a $\text{TiO}_2(110)$ surface [17]. The study showed that the AFM and STM signatures of the surface and subsurface defects were distinctly different due to the different nature and range of forces probed in AFM compared to the tunnel current in STM, which is dependent on the local electronic structure of the surface and influenced by subsurface defects. The study demonstrates that dual-channel imaging may be useful for analyzing the atomic-scale configuration of important subsurface defects such as subsurface H, O vacancies and dopant atoms in other metal oxides. However, in order to develop dual AFM/STM as a fully reliable tool it is important to understand which are the main components important for an accurate simulation. In this work, we build on the above-mentioned previous studies and analyze in detail the components qualitatively and quantitatively important in combined STM and nc-AFM measurements on the ideal and defective $\text{TiO}_2(110)$ surface. In particular, we consider how the tip size, shape and orientation relative to the scanning direction influences the measured contrast and tunneling current on the ideal TiO_2 surface. We then investigate the role of exchange-correlation functional and tip-surface relaxation when simulating imaging of defects on the surface. Finally, we study how surface and subsurface defects themselves can influence the measurements even when not directly under the tip.

2. Methods

2.1. Experimental details

The set-up for the experiments were comprised of a standard ultra-high vacuum (UHV) chamber with a base pressure below 1×10^{-10} and an Omicron VT-AFM enhanced with a digital EasyPLL Plus electronics (Nanosurf) for frequency detection. All experiments reported here were carried out at room temperature on a clean $\text{TiO}_2(110)$ single-crystal surface exposing the regular (1×1) termination [18]. The $\text{TiO}_2(110)$ surface was prepared prior to the experiments using Ar^+ ion bombardment ($E = 800$ eV, fluence 1×10^{16} cm^{-2}) followed by annealing at ~ 950 K for 20 min. For AFM imaging, we used highly doped Si cantilevers (Nanosensors type NCH,

$f_0 \sim 300$ kHz), which were initially treated with a light Ar^+ ion bombardment required to remove the native silicon oxide layer and render the tip's apex conducting for STM imaging. The bias voltage (U_{bias}) applied to the surface relative to the tip (grounded) was monitored regularly and adjusted to minimize the electrostatic forces arising from the contact potential difference (CPD). It was observed that the CPD changed significantly, ranging from a value of 2.3 V for a new tip to 0.51 V for a tip cleaned with the Ar^+ ion bombardment, a change which we attribute to the removal of the oxide layer on the tip. Tunneling currents are measured on the tip with a separate preamplifier suitable for low-current STM operation (Omicron SPM Preamp ver 4). A further detailed account for the experimental set-up, the operation of the nc-AFM and parameters for the $\text{TiO}_2(110)$ surface preparation is described in [19].

Before we discuss the experimental results, it is important to point out that the experimental images were recorded in the topographic nc-AFM mode (Z channel), where the tip traces the surface on contours of a predetermined constant frequency shift. The tunneling current (I_t channel) was recorded simultaneously as an additional passive signal and stored in a separate channel. This experimental protocol was adopted since the instrumental stability was better compared to scanning in constant height. When the I_t is recorded during nc-AFM experiments in this manner, it is important to note that the magnitude of the measured current signal is modulated by the oscillation of the cantilever in and out of tunneling, and by the motion of the tip apex determined by the Δf feedback setting. However, as described previously in [14] using the topographic trace of the nc-AFM tip, it is rather straightforward to extract and compare directly experimental values with simulated values, and we will apply this procedure here. Further details concerning the experimental recording of simultaneous STM and nc-AFM images and the analysis of such data have been presented in detail in [14].

2.2. Theoretical

Density functional theory (DFT) calculations have been performed using the plane wave basis Vienna *ab initio* simulation package (VASP) [20, 21], implementing projected augmented wave (PAW) potentials [22] (for Ti, the 3s and 4p semicore states are considered as valence states). Using a kinetic cutoff energy of 450 eV and a Γ centered Monkhorst-Pack grid with 0.04 \AA^{-1} spacing between k points (e.g. this is equivalent to $5 \times 5 \times 8$ and $2 \times 2 \times 1$ grids of the corresponding primitive cell of bulk rutile TiO_2 and $\text{TiO}_2(110)$ - (2×4) slab, respectively), we converge the total energy to < 1 meV/atom. All the structures under study were fully relaxed until all the forces were < 0.01 eV \AA^{-1} . Simulated STM images were performed using multiple electron scattering with a Green's function formalism implemented in the bSKAN code [14, 23].

In this work we computed the average STM current considering the AFM trajectory of the tip. For instance, in our case, the tip is oscillating with some frequency, ν , and peak-to-peak amplitude, $A_{\text{p-p}}$, along the $[110]$ axis. The maximum tip-surface approach at a certain point in the plane is given by

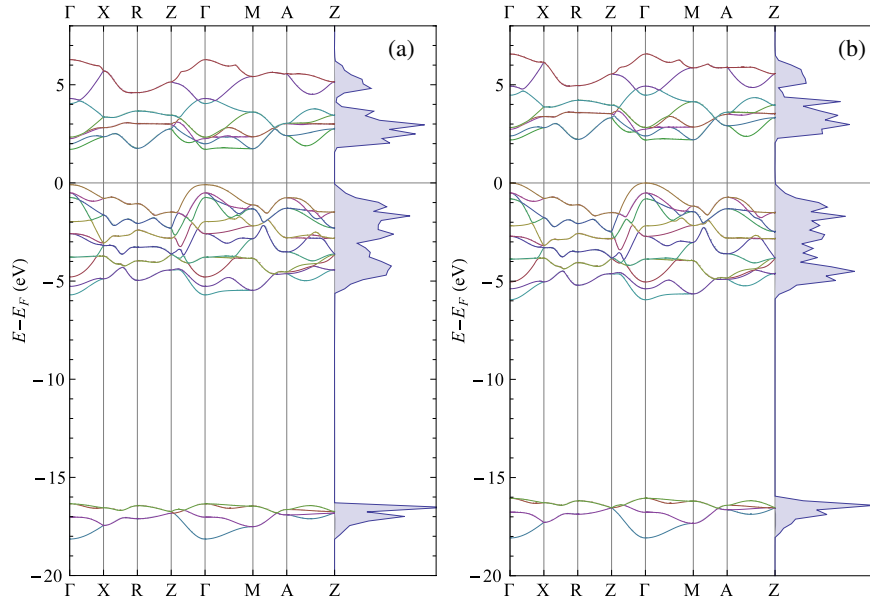


Figure 1. Computed (a) PBE and (b) LDA + U band structure.

$Z = Z(x, y)$, then the tip's trajectory can be expressed like $z[x, y, t] = Z(x, y) + \zeta(v, A_{p-p}, t)$. Thus the average STM current should be

$$\langle I_{\text{STM}} \rangle = I_t(x, y) = v \int_0^{1/v} dt I_{\text{STM}}[x, y, z(x, y, t)]. \quad (1)$$

Note that a further difference in this work to previous studies of STM imaging of the TiO_2 surface with similar methods, e.g. [24], aside from the coupling to simultaneous AFM, is the inclusion of a realistic tip in simulations, which we found essential to reproduce experimental results.

2.2.1. Functional choice. The choice of exchange–correlation function for studying the $\text{TiO}_2(110)$ surface remains a controversial issue due to uncertainties in the correct description of defect states [25]. However, the latest results seem to support the use of vanilla DFT for the ideal surface, while hybrid functionals or on-site Coulomb corrections are better suited to treating the defective surface [25–28]. We use the generalized gradient approximation by Perdew, Burke and Ernzerhof (PBE) [29] for computing the electronic and structural properties of clean $\text{TiO}_2(110)$ and both the Si- and W-based tips. In the case of defective $\text{TiO}_2(110)$ we used the local spin polarized approximation with an on-site Coulomb interaction between Ti 3d electrons in Dudarev's approach [30] (LSDA + U). Later in the paper we discuss the influence of this choice on the calculated current and simulated images.

The PBE-computed lattice parameters for bulk TiO_2 are $a_{\text{PBE}} = 4.654 \text{ \AA}$, $c_{\text{PBE}} = 2.973 \text{ \AA}$ and $u_{\text{PBE}} = 0.305$ and the bulk modulus $K_{\text{PBE}} = 202.7 \text{ GPa}$. These values are in good agreement with experimental ones: $a_{\text{Expt}} = 4.5936 \text{ \AA}$, $c_{\text{Expt}} = 2.9587 \text{ \AA}$, $u_{\text{Expt}} = 0.3048$ [31] and $K_{\text{Expt}} = 212 \text{ GPa}$ [32]. For LSDA + U calculations, we adjusted $U = 3.6 \text{ eV}$ to reproduce the experimental bulk cell volume of 62.432 \AA^3 [31]. This corresponds to the

LSDA + U computed lattice parameters: $a_{\text{LSDA}+U} = 4.584 \text{ \AA}$, $c_{\text{LSDA}+U} = 2.971 \text{ \AA}$ and $u_{\text{LSDA}+U} = 0.3042$. In figure 1 we display the computed PBE and LDA + U electronic structure; both are fundamentally similar but with different bandgaps: 1.7 (2.2) eV for PBE (LDA + U). Although the LDA + U bandgap value is smaller in comparison with the experimental 3.0 eV bandgap [33], it is in qualitatively good agreement with a recent hybrid DFT (PBE0) computation [25]—the dispersion of the conduction bands are similar.

2.2.2. Tip–surface set-up. The $\text{TiO}_2(110)$ surface (see figure 2) was modeled by several slabs, all of them with five ‘trilayers’ (O– TiO_2 –O) (freezing the lowest two trilayers during relaxation) and a 15 \AA vacuum along the [110] direction. Previous studies have shown that bond lengths in $\text{TiO}_2(110)$ are properly described by slabs with at least five trilayers [34], although only slabs with more than 11 trilayers should achieve convergent surface energy and absolute ionic positions [34]. Using dipolar corrections and the same convergency criteria as in the bulk, the $\text{TiO}_2(110)$ –(1 × 1) surface structure within both approximations (PBE and LDA + U) is practically the same as in [24] and is in good agreement with recent high resolution low energy electron diffraction measurements (LEED-IV) [35]. We use these slabs as the basis for other surface reconstructions.

In figure 3 we display three structurally different silicon-based tips considered specifically in this work (although many others, including hydroxyl termination, are detailed in [14]). Since in AFM experiments the tip usually contacts the surface, the tip nanoapices are most often either ‘clean’ or a mixture of Si atoms with some Ti_xO_y nanoclusters. In the same fashion as TiO_2 , we computed the structural and electronic properties of these tips using PBE (allowing full relaxation of the nanoapex). As previous studies have shown that modeling the tip structure with some pyramidal shape can reproduce satisfactorily the

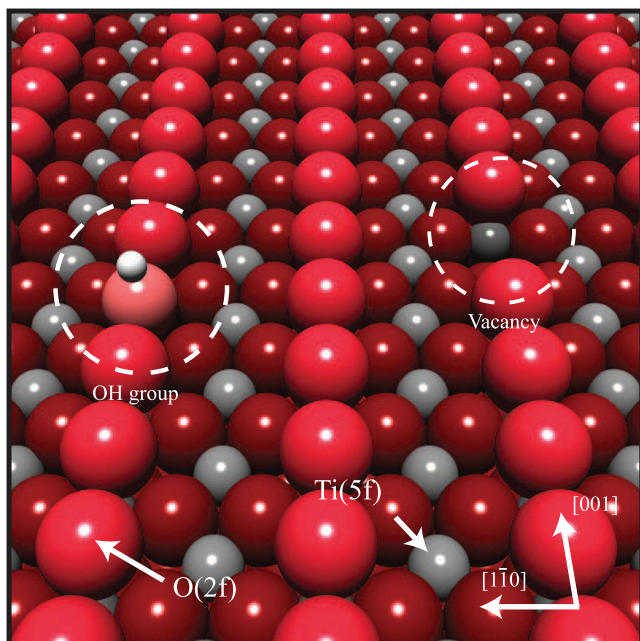


Figure 2. Ball model of the $\text{TiO}_2(110)$ surface. The surface exposes fivefold-coordinated Ti(5f) atoms in the troughs and protruding twofold-coordinated bridging O(2f) atoms. Also indicated is a bridging hydroxyl group (sOH) and an oxygen vacancy. Color code—Ti: small light grey and O: red (dark grey and large light grey).

observed corrugation and STM currents [36, 37], we built our tips maintaining some pyramidal structure.

3. Results

To illustrate our approach used to determine the atomistic tip apex nature, figure 4 shows two examples of simultaneously recorded nc-AFM (z) and STM (I_t) images of the hydroxylated $\text{TiO}_2(110)$ surface. In this state, the $\text{TiO}_2(110)$ surface exposes a structure consisting of alternating Ti rows and O rows consisting of twofold-coordinated bridge-bonded oxygen atoms. Additionally, the surface exhibits a low concentration of bridging surface OH groups that are located on the oxygen rows [38, 39]. The non-contact AFM images in figures 4(a) and (d) are recorded with two distinctly different tip terminations, as evidenced by the position of the bright rows relative to the surface OH groups (sOH). In figure 4(a), the sOH groups are clearly located directly on the dark rows.

This demonstrates that the Ti rows are imaged bright and the oxygen rows are dark with this particular tip termination, reflecting that the attractive contribution of the tip surface force is at a maximum over Ti. In figure 4(d), the situation is clearly different and now the atomic protrusions associated with the sOH groups are located directly on the bridging O rows, signifying that the force is at a maximum here. A third contrast mode (not shown) is also possible, where the O rows appear bright with sOH imaged as depressions on the O rows [19]. These three distinctly different nc-AFM contrast modes can be explained by a tip contribution depending on the polarity of the localized chemical force between the surface and a tip terminated by either an electropositive (O-terminated), electronegative (Ti-terminated) or neutral nanoapex (Si), respectively. Figure 4(a) thus represents a typical image taken with a negatively terminated tip since the force is maximum over the Ti rows, whereas the contrast pattern seen in figure 4(d) closely represents the geometry of the surface imaged with a neutral tip.

Figures 4(a), (b), (d) and (e) are sets of simultaneously recorded AFM (Z) and STM (I_t) images recorded with a negative tip or a neutral tip termination, respectively. For the negative tip (figures 4(a) and (b)), an analysis of parallel linescans in figure 4(c) shows that the corrugation is ‘in-phase’, showing that the Ti rows are imaged as bright in the I_t image even though the tip here retracted from the surface. This indicates that the point of maximum attractive forces in AFM and the point of maximum tunneling probability in STM coincide over the Ti rows. In the second illustration (figures 4(d) and (e)), the linescan in figure 4(f) shows that the signal is also ‘in-phase’ here, but the situation is opposite from the negative tip since now the point of maximum attractive forces is on the O rows and, correspondingly, the point of maximum tunneling probability is also on the O rows. A main conclusion is therefore that the imaging contrast in simultaneous atom-resolved STM and AFM experiments is crucially dependent on the exact tip structure both on a qualitative and quantitative level [14], and that accurate simulation of STM as well as AFM requires accurate atomistic tip models. However, as demonstrated in [14], having access to both AFM and STM signals makes it possible first to establish the type of charge (negative, positive or neutral) on the nanoapex of the tip [19] and then model theoretically the tunneling properties of a very limited number of tips with such properties and determine the STM contrast of the TiO_2 surface and its defects.

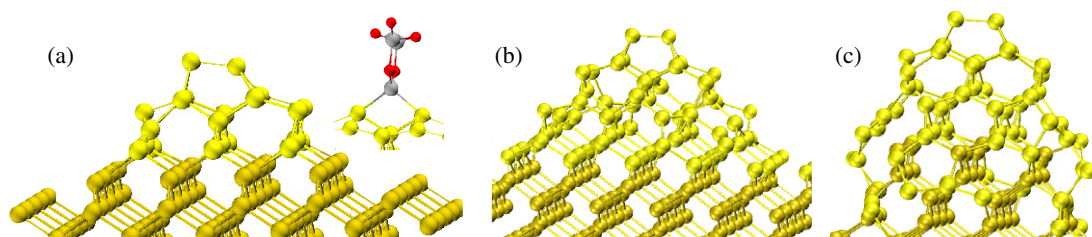


Figure 3. Tip structures computed in this work: (a) default dimer tip, with inset showing a possible Ti_3O_5 nanoapex, (b) large dimer tip, with twice as many atoms in both the fixed and relaxed part of the tip, and (c) narrow dimer tip, with less atoms in the base of the tip. Here yellow (large dark grey), red (small dark grey) and light grey spheres stand for Si, O and Ti, respectively.

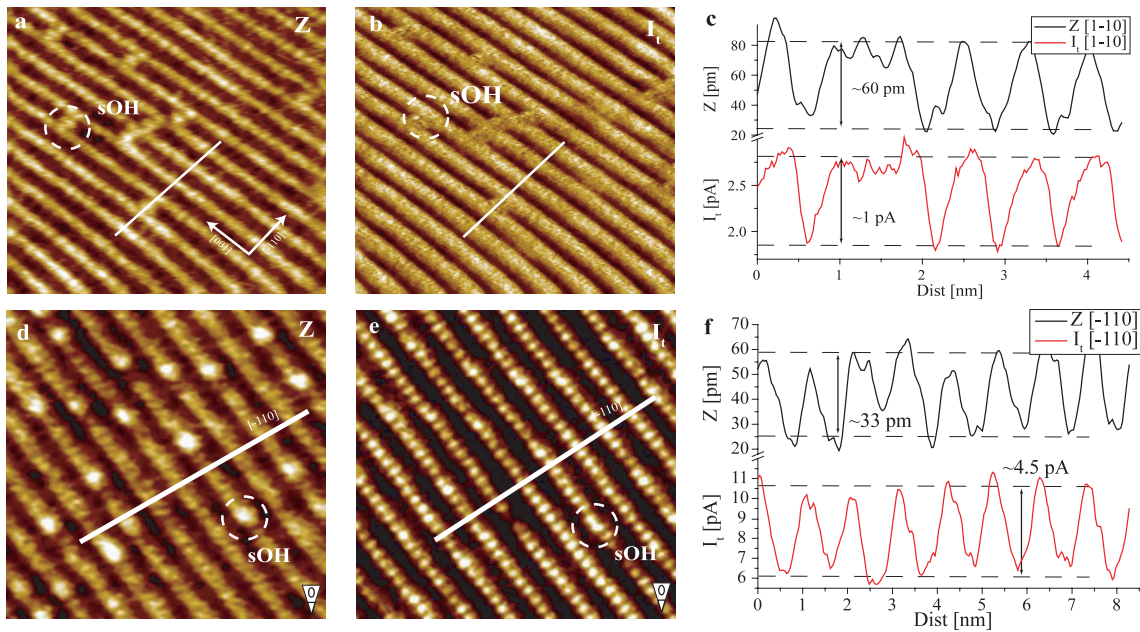


Figure 4. Experimentally recorded simultaneous AFM (Z) and STM (I_t) data and associated linescans recorded with two different tip terminations. The sequence ((a)–(c)) reflects a negatively charged O-terminated tip. Imaging parameters: size = $10 \times 10 \text{ nm}^2$, $df = -46.9 \text{ Hz}$, $U_{\text{bias}} = 0.97 \text{ V}$ and $A_{\text{p-p}} = 26 \text{ nm}$. The sequence ((d)–(f)) reflects data recorded with a neutral Si-terminated tip. Imaging parameters were: size = $10 \times 10 \text{ nm}^2$, $df = -53 \text{ Hz}$, $U_{\text{bias}} = 0.97 \text{ V}$ and $A_{\text{p-p}} = 26 \text{ nm}$.

3.1. Tip size and orientation

In [14] we proposed ten structurally different tips. Starting from those results, here we study the effect of size and orientation of the tip on I_t . We simplify our studies by considering only the neutral mode imaging (see figure 4(d) and section 2). As the polarity of the different surface ions no longer dominates the interactions with the AFM tip, this tip might be purely Si-based [14, 40]. Our previous results suggest that an ‘out-of-phase’ I_t image can be explained by an Si tip with Si dimer apex (cf figure 11 in [14]), allowing us to focus on the three silicon tips shown in figures 3(a)–(c).

In figure 5(a1) we display the computed average STM current along the AFM trajectory for tip-(a). The Si dimer apex orientation is parallel to the $[\bar{1}10]$ surface axis. In figure 5(a2) we also display the linescan along $[\bar{1}10]$ starting from the origin of figure 5(a1). In the I_t image, the bright rows indicate the location of the Ti(5c) rows; this has some double imaging related to the orientation of the Si dimer and its asymmetry (one of the Si is closer to the surface). It is clear that tunneling occurs to both Si atoms. After rotating the tip by 90° , we find an improvement of the I_t image in figure 5(b1) with respect to the experiment. The corresponding linescan (figure 5(b2)) shows an increment of I_t magnitude by three times in comparison to figure 5(a2). A similar increase in current magnitude with orientation can be seen by comparing scanlines, figures 6(a2) and (b2). However, the use of a larger tip has two further more general effects: firstly, the blunter tip loses some resolution and the secondary features seen in figures 5(a1) and (a2) disappear; secondly, we see almost an order of magnitude increase in current. This dependence of current on tip size and shape can be clearly seen with the sharp tip, figure 3(c), which provides the smallest current of all

the tips considered here (figure 7(a2)), while still not offering any significant increase in the number of atomic sites clearly resolved (figure 7(a1)).

3.2. Exchange–correlation functional

As discussed in section 2.2.1, earlier studies have considered the role of different exchange–correlation functionals for calculating the electronic structure of the ideal and defective $\text{TiO}_2(110)$ surfaces. The key issue is the position of the conduction band and defect levels in the gap and the associated, localization of electron density associated with defect states. As for most materials, vanilla DFT underestimates the bandgap of TiO_2 , but this does not prevent the approach from providing very good physical accuracy for the surface [18]. For defect states, the underestimation of the bandgap generally leads to defect states lying too close to the conduction band and becoming artificially delocalized [25–28].

In order to study the influence of this problem on simultaneous AFM–STM imaging of defects on the surface, we calculated scanlines over sOH and subsurface hydrogen (OH_{sub}) defects on the $\text{TiO}_2(110)$ surface—impurities seen in experimental images [14, 17]. For images of the defective surface, the most common experimentally obtained image contrast [14] was linked to a silicon tip contaminated by TiO_2 . Hence, for the comparison of images of defects in the surface we use the Si(001)– Ti_3O_5 O-terminated tip [001] aligned, as shown in the inset in figure 3(a). This tip’s primary tunneling site is the five-coordinated Ti ions in the surface, and these are resolved as bright rows in images [14]. Figure 8 shows the calculated results for PBE and LSDA + U .

Analyzing the electronic structure, we find that, as expected, the defect state is much more delocalized in the

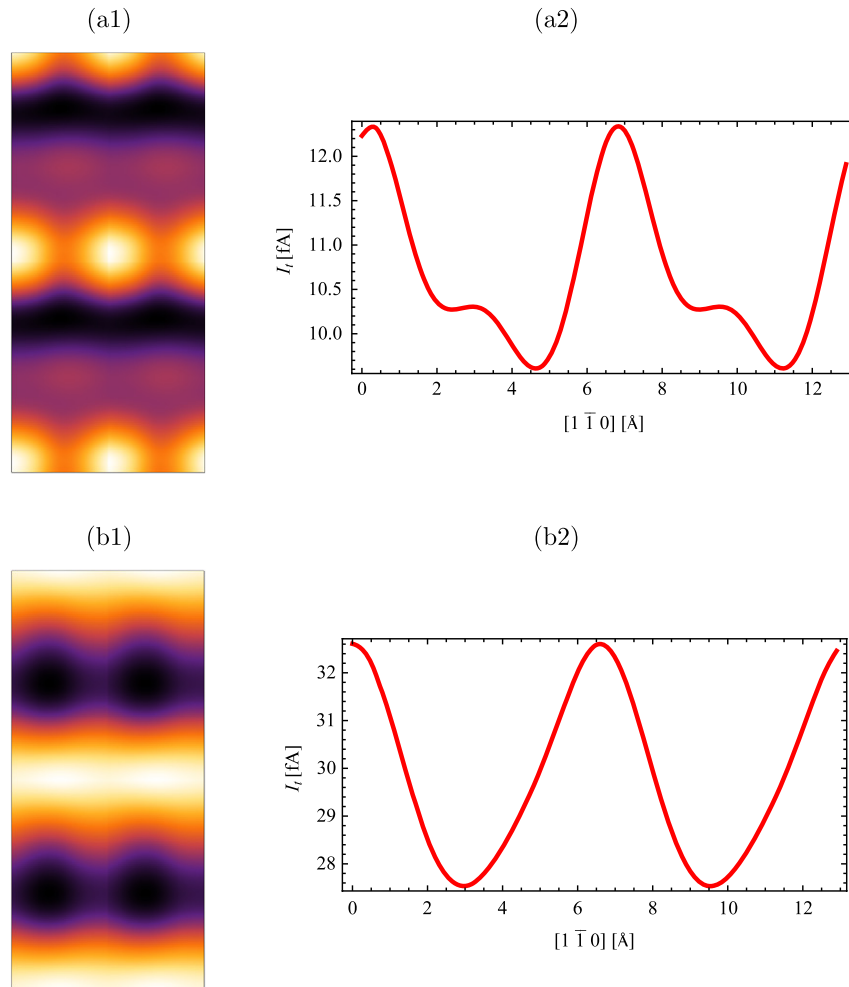


Figure 5. Computed I_t for tip (a) on $\text{TiO}_2(110)$ when the Si dimer apex is oriented along (a) $[\bar{1}10]$ and (b) $[001]$ with respect to the surface. The linescans are along the $[110]$ surface axis starting from the origin of the corresponding I_t image. The STM currents were computed using $V_{\text{bias}} = 1.0$ V and maximum approach surface–tip 5 Å.

PBE approximation. In fact, for the sOH, the density of the defect state is delocalized across the whole imaging cell and figure 8(a) shows that resolution of the neighboring Ti rows is now lost. The sOH site would dominate in STM images up to nanometers from the actual defect site—this is not observed in any experiments. The sOH should appear, with this tip, as a bright contrast in-between bright rows, as shown in figure 4. Using LSDA + U increases the TiO_2 gap (see figure 1) and the hydrogen defect level decouples from the conduction band, forming a localized state. Figure 8(b) shows the sOH is now resolved as a bright contrast in-between bright Ti rows, exactly as in the experiments. For OH_{sub} similar problems within PBE occur due to delocalization and we actually see contrast reversal near the defect site—figure 8(a) shows that there is now less current over the Ti row than the bridging oxygen row. LSDA + U returns maximum contrast to the Ti row and resolves the OH_{sub} as a perturbation in-between the Ti rows, as seen in experiments [17]. More generally, the use of LSDA + U , and the resulting localization of defect states, leads to an order of magnitude increase in average current for a given tip position.

3.3. Tip–surface relaxations

The influence of surface and tip relaxations on the STM current was modeled following the ideas of [41]. We studied the case of an $\text{Si}(001)$ – Ti_3O_5 O-terminated tip interacting with $\text{TiO}_2(110)$. As the size of the tip and the required thickness of the $\text{TiO}_2(110)$ slab would require a huge system to relax, we tackle the problem considering just the topmost part of the tip: one layer of $\text{Si}(001)$ (passivated with H atoms) attached to a Ti_3O_5 cluster. During the tip–surface approach, only the three topmost trilayers of $\text{TiO}_2(110)$ and the Ti_3O_5 cluster were allowed to relax. We used the outcome of this deformation to modify the corresponding coordinates of the original tip and $\text{TiO}_2(110)$ surface, and thus we computed the wavefunctions of the deformed tip and surface separately. Those wavefunctions were then used to compute the STM currents using bSKAN as described above.

In figure 9 we plot the computed I_t linescan along the $[\bar{1}10]$ axis across the OH site. In general, we observed that surface and tip relaxations are <0.05 Å when the tip is ~ 3.0 Å above O_1 . When the tip is 2.1 Å above O_1 , we see that the tip–surface interaction induces 19° bending on the nanoapex along the $[001]$ direction with a 0.01 Å relaxation of O_1 . When

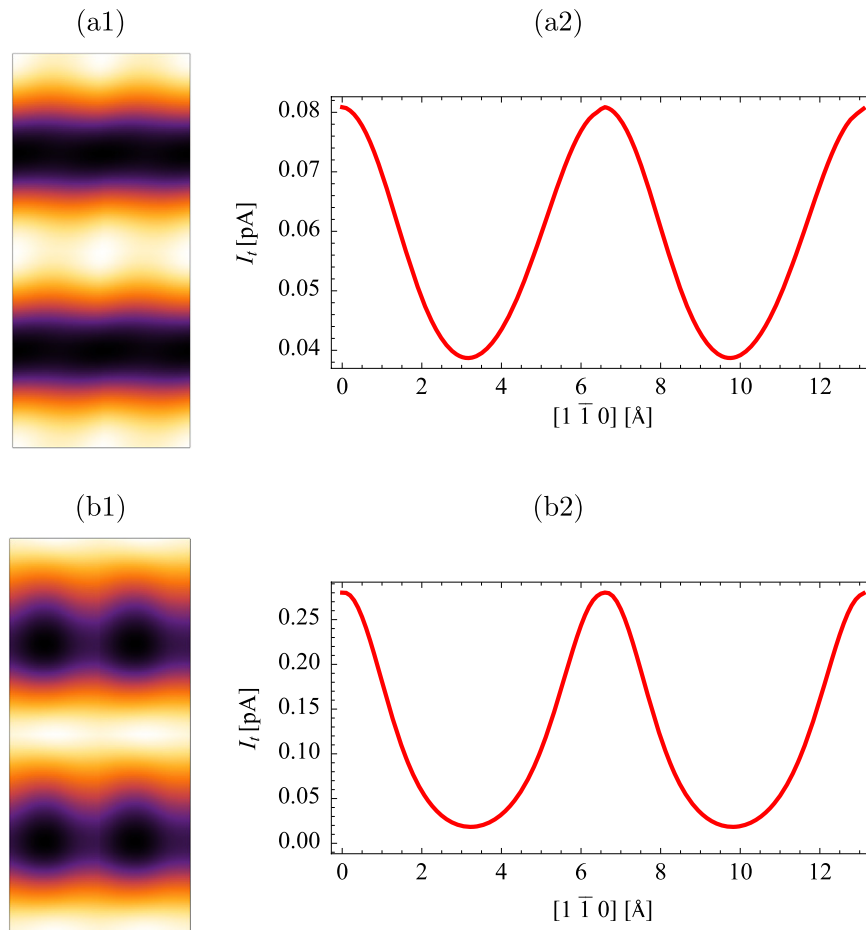


Figure 6. Computed I_t for tip (b) on $\text{TiO}_2(110)$ when the Si dimer apex is oriented along (a) $[\bar{1}10]$ and (b) $[001]$ with respect to the surface. The linescans are along the $[110]$ surface axis starting from the origin of the corresponding I_t image. The STM currents were computed using $V_{\text{bias}} = 1.0$ V and maximum approach surface–tip 5 Å.

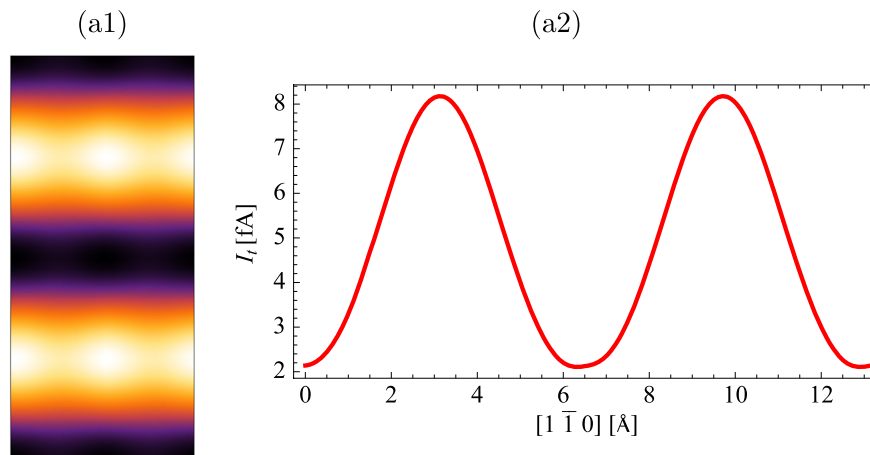


Figure 7. Computed I_t for tip (c) on $\text{TiO}_2(110)$ when the Si dimer apex is oriented along $[\bar{1}10]$. The linescan is along the $[\bar{1}10]$ surface axis starting from the origin of the corresponding I_t image. The STM currents were computed using $V_{\text{bias}} = 1.0$ V and maximum approach surface–tip 5 Å.

the tip is at 3.9 Å above the Ti_1 site, the apex O relaxes 0.1 Å towards the surface and Ti_1 relaxes ~ 0.1 Å towards the tip. The inclusion of these relaxation effects leads to an increase in average current of about 50%, but otherwise does not change the characteristic contrast pattern.

3.4. Characteristic defects

For standard preparation conditions, the three most probable defects present at, or near, the surface are: bridging oxygen vacancies [18], hydroxyl groups [16, 38] and Ti interstitials [42]. Here we do not consider direct imaging

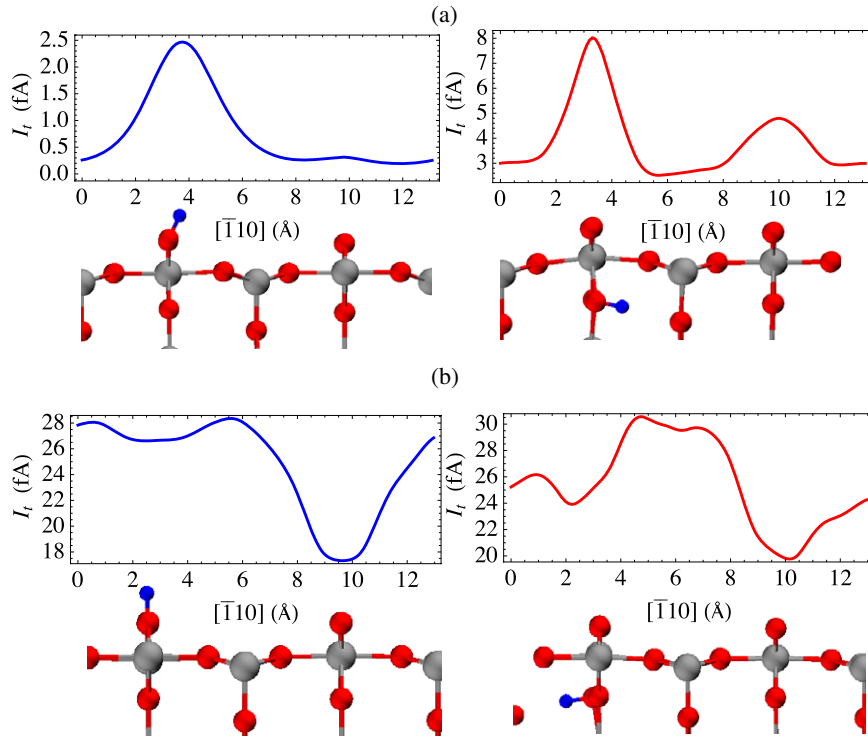


Figure 8. I_t for Si(001)–Ti₃O₅ O-terminated tip and $V_{\text{bias}} = 0.5$ V using (a) the PBE approximation and (b) LSDA + U for modeling TiO₂(110) with sOH and OH_{sub}. Note that we show energetically identical positions of the OH_{sub} site in (a) and (b)—there is no significant difference in ground-state geometry between PBE and LSDA + U . The barrier for the rotation of H between these two sites is over 1 eV. In all the linescans, the minimum tip–surface distance is 2.4 Å at the O bridging sites or the sOH position.

of these defects, but rather investigate how the presence of neighboring defects or impurities can also influence the local imaging conditions. In figure 9 we compare scanlines for three defect ‘sets’ for the same minimum tip–surface distance, using the same Si(001)–Ti₃O₅ O-terminated tip. The scanline for OH_{sub} is the same as shown in figure 8 and is included for reference. The Ti interstitial results in a shift of the maximum current slightly off the position of the Ti row, reflecting the contribution of tunneling into the interstitial site. It also results in a general reduction in the magnitude of measured current around the defect site. The oxygen vacancy causes little change in the appearance of the OH_{sub} in the scanline, but the increased conductivity of the reduced surface provides a general increase in average current.

4. Conclusions

The main conclusion of this work is that simulations of dual-channel measurements require consideration of several factors normally ignored in single-channel measurements. In nc-AFM measurements, simulations are principally concerned with reproducing the chemical forces between the tip and surface, and these are dominated by the nature of the tip apex and the local surface properties. The dependence of forces on the exchange–correlation functional is much weaker, since they both provide the same ground-state structures. Subsurface defects tend to be heavily screened by the surface atoms and have little influence on nc-AFM contrast. The large-scale

properties of the tip play little role in the chemical forces, aside from increasing relaxation degrees of freedom and background van der Waals forces. Similarly, for simulations of STM alone, we are interested only in reproducing the local tunneling current versus bias dependence measured in experiments. Conventional STM experiments scan much further from the surface than nc-AFM due to the difference in decay length of the relevant signals ($\sim 5\text{--}6$ Å compared to $\sim 3\text{--}4$ Å), so tip–surface relaxations can safely be neglected. STM at this range also tends to be less sensitive to the tip apex.

In combined STM–AFM studies, our results show that simulations must account for all these factors in both modes, or at least understand the errors present in neglecting them. We demonstrate that the tip size and orientation is a critical component in the calculated current, with larger tips in registry with tunneling sites in the surface, providing orders of magnitude increases. The exchange–correlation functional used is, of course, critical in obtaining a correct description of the electronic structure of the surface, and particularly defects, and this has a strong influence on the simulated contrast and current. Tip–surface relaxations and the presence of neighboring defects and impurities also contribute to simulated current values, although, for this system, the changes to contrast patterns were small. Taking into account all these factors upgrades the qualitative agreement with experiments seen in earlier studies [14, 17] to quantitative agreement, and re-emphasizes the power of multi-channel modes for studying surfaces in high resolution.

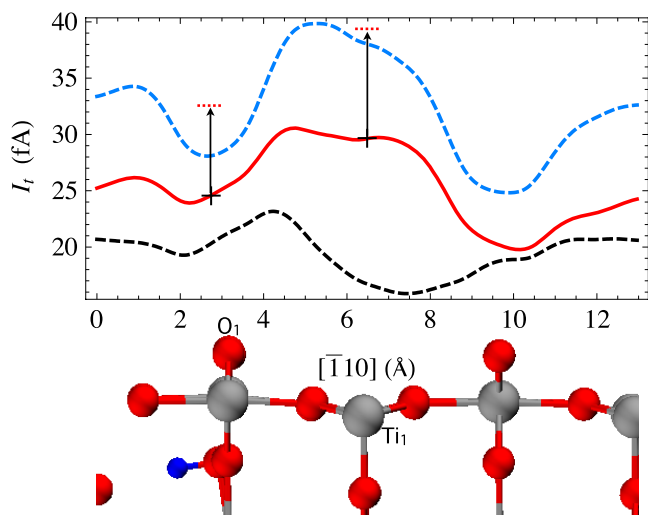


Figure 9. LSDA + U computed I_t linescans at $V_{\text{bias}} = 0.5$ V of the $\text{TiO}_2(110)$ surface with an $\text{Si}(001)\text{-Ti}_3\text{O}_5$ O-terminated tip across: an isolated OH_{sub} (red solid line); an OH_{sub} and neighboring $\text{Ti}_{\text{interst}}$ (lower dashed black line); and an OH_{sub} and neighboring O_{vac} (higher dashed blue line). Note that the $\text{Ti}_{\text{interst}}$ and O_{vac} are far from the OH_{sub} site and are not shown in the structural figure. For the case of $\text{TiO}_2(110)$ with an isolated OH_{sub} we consider also the effect of tip–surface relaxations at two sites indicated by the black crosses. When the $\text{Si}(001)\text{-Ti}_3\text{O}_5$ tip is just above O_1 (Ti_1), I_t increases to 32.7 (39.4) fA. All the linescans were computed considering a tip–surface maximum approach of 2.4 Å that is at the O bridging sites. The relaxation effect was computed placing the tip at two positions: 2.1 Å and 3.9 Å above O_1 and Ti_1 sites, respectively.

Acknowledgments

ASF and HPP acknowledge support from the Academy of Finland through its Center of Excellence program and generous grants of computing time from the Center for the Scientific Computing (CSC), in Espoo, Finland. The iNANO group acknowledges generous support from Haldor Topsøe A/S, and the Carlsberg and Lundbeck Foundations.

References

- [1] Morita S, Wiesendanger R and Meyer E (ed) 2002 *Noncontact Atomic Force Microscopy* (Berlin: Springer)
- [2] Hofer W, Foster A S and Shluger A L 2003 *Rev. Mod. Phys.* **75** 1287
- [3] Bennowitz R, Foster A S, Kantorovich L N, Bammerlin M, Loppacher C, Schär S, Guggisberg M, Meyer E and Shluger A L 2000 *Phys. Rev. B* **62** 2074
- [4] Zerweck U, Loppacher C, Otto T, Grafström S and Eng L M 2005 *Phys. Rev. B* **71** 125424
- [5] Barth C and Henry C R 2006 *Appl. Phys. Lett.* **89** 252119
- [6] Barth C and Henry C R 2007 *Phys. Rev. Lett.* **98** 136804
- [7] Enevoldsen G H, Glatzel T, Christensen M C, Lauritsen J V and Besenbacher F 2008 *Phys. Rev. Lett.* **100** 4
- [8] Loppacher C, Bammerlin M, Guggisberg M, Schär S, Bennowitz R, Baratoff A, Meyer E and Güntherodt H J 2000 *Phys. Rev. B* **62** 16944
- [9] Özer H O, O'Brien S J and Pethica J B 2007 *Appl. Phys. Lett.* **90** 133110
- [10] Ternes M, Lutz C P, Hirjibehedin C F, Giessbl F J and Heinrich A J 2008 *Science* **319** 1066
- [11] Kantorovich L N and Trevethan T 2004 *Phys. Rev. Lett.* **93** 236102
- [12] Bocquet F, Nony L, Loppacher C and Glatzel T 2008 *Phys. Rev. B* **78** 035410
- [13] Jelinek P, Svec M, Pou P, Perez R and Chab V 2008 *Phys. Rev. Lett.* **101** 176101
- [14] Enevoldsen G H, Pinto H, Foster A S, Christensen M C, Kühnle A, Reichling M, Hofer W, Lauritsen J V and Besenbacher F 2008 *Phys. Rev. B* **78** 045416
- [15] Suzuki S, Fukui K, Onishi H and Iwasawa Y 2000 *Phys. Rev. Lett.* **84** 2156
- [16] Lauritsen J V, Foster A S, Olesen G H, Christensen M C, Kühnle A, Helveg S, Rostrup-Nielsen J R, Clausen B S, Reichling M and Besenbacher F 2006 *Nanotechnology* **17** 3436
- [17] Enevoldsen G H, Pinto H P, Foster A S, Jensen M C R, Hofer W A, Hammer B, Lauritsen J V and Besenbacher F 2009 *Phys. Rev. Lett.* **102** 136103
- [18] Diebold U 2003 *Surf. Sci. Rep.* **48** 53
- [19] Enevoldsen G H, Foster A S, Christensen M C, Lauritsen J V and Besenbacher F 2007 *Phys. Rev. B* **76** 205415
- [20] Kresse G and Furthmüller J 1996 *Phys. Rev. B* **54** 11169
- [21] Kresse G and Furthmüller J 1996 *Comput. Mater. Sci.* **6** 15
- [22] Kresse G and Joubert J 1999 *Phys. Rev. B* **59** 1758
- [23] Palotás K and Hofer W A 2005 *J. Phys.: Condens. Matter* **17** 2705
- [24] Teobaldi G, Hofer W, Bikondoa O and Pang C 2007 *Chem. Phys. Lett.* **437** 73
- [25] Labat F, Baranek P, Domain C, Minot C and Adamo C 2007 *J. Chem. Phys.* **126** 154703
- [26] Valentin C D, Pacchioni G and Selloni A 2006 *Phys. Rev. Lett.* **97** 166803
- [27] Calzado C J, Hernandez N C and Sanz J F 2008 *Phys. Rev. B* **77** 045118
- [28] Mattioli G, Filippone F, Alippi P and Amore Bonapasta A 2008 *Phys. Rev. B* **78** 241201
- [29] Perdew J P, Burke K and Ernzerhof M 1996 *Phys. Rev. Lett.* **77** 3865
- [30] Dudarev S L, Botton G A, Savrasov S Y, Humphreys C J and Sutton A P 1998 *Phys. Rev. B* **57** 1505
- [31] Abrahams S C and Bernstein J L 1971 *J. Chem. Phys.* **55** 3206
- [32] Isaak D G, Carnes J D, Anderson O L, Cynn H and Hake E 1998 *Phys. Chem. Miner.* **26** 31
- [33] Kavan L, Gratzel M, Gilbert S, Klemenz C and Scheel H 1996 *J. Am. Chem. Soc.* **118** 6716
- [34] Thompson S J and Lewis S P 2006 *Phys. Rev. B* **73** 073403
- [35] Swamy V, Muscat J, Gale J D and Harrison N M 2002 *Surf. Sci.* **504** 115
- [36] Hofer W A, Redinger J and Podloucky R 2001 *Phys. Rev. B* **64** 125108
- [37] Hofer W A 2003 *Prog. Surf. Sci.* **71** 147
- [38] Wendt S *et al* 2005 *Surf. Sci.* **598** 226
- [39] Bikondoa O *et al* 2006 *Nat. Mater.* **5** 189
- [40] Enevoldsen G H, Foster A S, Christensen M C, Lauritsen J V and Besenbacher F 2007 *Phys. Rev. B* **76** 205415
- [41] Hofer W A, Fisher A J, Wolkow R A and Grütter P 2001 *Phys. Rev. Lett.* **87** 236104
- [42] Wendt S *et al* 2008 *Science* **320** 175